

Melting of the orbital order in LaMnO₃ probed by NMR

A. Trokiner,¹ S. Verkhovskii,^{1,2} A. Gerashenko,^{1,2} Z. Volkova,²
O. Anikeenok,³ K. Mikhalev,² M. Eremin,³ and L. Pinsard-Gaudart^{4,5}

¹*LPEM, ESPCI ParisTech, UMR 8213, CNRS, 75005 Paris, France*

²*Institute of Metal Physics, Ural Branch of Russian Academy of Sciences, 620041 Ekaterinburg, Russia*

³*Institute of Physics, Kazan Federal University, 420008 Kazan, Russia*

⁴*Univ. Paris-Sud, Institut de Chimie Moléculaire et des Matériaux d'Orsay, UMR8182, Bat. 410, Orsay 91405 France*

⁵*CNRS, Orsay, 91405 France*

(Dated: June 8, 2022)

The Mn spin correlations were studied near the $O'-O$ phase transition at $T_{JT} = 750$ K, up to 950 K with ^{17}O and ^{139}La NMR in a stoichiometric LaMnO₃ crystalline sample. The measured local hyperfine fields originate from the electron density transferred from the e_g - and t_{2g} -orbitals to the $2s(\text{O})$ and $6s(\text{La})$ orbits, respectively. By probing the oxygen nuclei, we show that the correlations of the Mn spins are ferromagnetic in the ab -plane and robust up to T_{JT} whereas along the c -axis, they are antiferromagnetic and start to melt below T_{JT} , at about 550 K. Above T_{JT} the ferromagnetic Mn–Mn exchange interaction is found isotropic. The room temperature orbital mixing angle, $\varphi_{\text{nmr}} = 109 \pm 1.5^\circ$, of the e_g ground state is close to the reported value which was deduced from structural data on Jahn-Teller distorted MnO₆ octahedra. For $T > T_{JT}$ LaMnO₃ can be described in terms of non-polarized e_g -orbitals since both e_g -orbitals are equally occupied.

PACS numbers: 75.25.Dk, 75.30.Et, 75.47.Lx, 76.60.-k

I. INTRODUCTION

The oxide LaMnO₃ is a key system for experimental and theoretical studies that aim to resolve the relative importance of the electron-electron (e - e) and electron-lattice (e - l) interactions for the orbital physics of manganites [1]. The orbital degree of freedom originates from the singly occupied degenerate e_g -state ($d_{3z^2-r^2} \equiv |\theta\rangle$, $d_{x^2-y^2} \equiv |\varepsilon\rangle$) of the Jahn-Teller (JT) active Mn³⁺ ($t_{2g}^3 e_g^1$) ions [2]. Owing to the coupling of orbital degrees of freedom with the lattice, at ambient conditions, in the O' -phase, the orthorhombic ($Pbnm$) structure of LaMnO₃ adopts a correlated pattern of corner-shared JT-distorted MnO₆ octahedra with long (l) and short (s) Mn–O bond lengths alternating in the ab -plane. This structural signature of the long-range orbital order (OO) involves the low-lying orbital state $|\psi_g\rangle = \cos(\varphi/2)|\theta\rangle + \sin(\varphi/2)|\varepsilon\rangle$ [3] which replicates the local symmetry of the oxygen environment at each Mn-site. Based on this correspondence, the room temperature value of the orbital mixing angle, φ , was estimated from MnO₆ octahedron distortions, $\varphi_{\text{str}} \sim 108^\circ$ [4]. This value is significantly smaller than 120° , the prediction of the JT model [3]; this points out the important role of the superexchange (SE) mechanism [2] in the spatial ordering of the occupied e_g -orbitals. The inclusion of the real structure of LaMnO₃ into the dynamic mean-field theory (DMFT) calculations [5, 6] has allowed getting $\varphi_{\text{dmft}} \sim 109^\circ$ at room T [6] taking into account both, e - l and e - e interactions.

According to DMFT, the e_g orbital state remains high-polarized even at $T > T_{JT} = 750$ K, where cooperative JT-distortions disappear [4]. In contrast to this prediction, Raman spectroscopy evidences that orbital-disorder fluctuations are present well below T_{JT} [7] indicating a

thermal instability of OO in the O' -phase [8]. The crystal structure of the high-temperature O -phase appears almost cubic on average [4], while dynamical JT distortions of the MnO₆ octahedra remain up to about 1150 K [9, 10].

Unfortunately, to date experimental structural information on OO [4, 7–10] has not much electronic counterpart. The OO provides a remarkable anisotropy of the effective exchange interaction [2], which explains the A-type antiferromagnetic (AF) spin order below $T_N \sim 140$ K [11, 12]. Moreover, the estimates of the exchange integral values [12] show that the AF exchange along the c -axis is weaker than the ferromagnetic (FM) exchange in the ab -layer. In the paramagnetic (PM) phase,

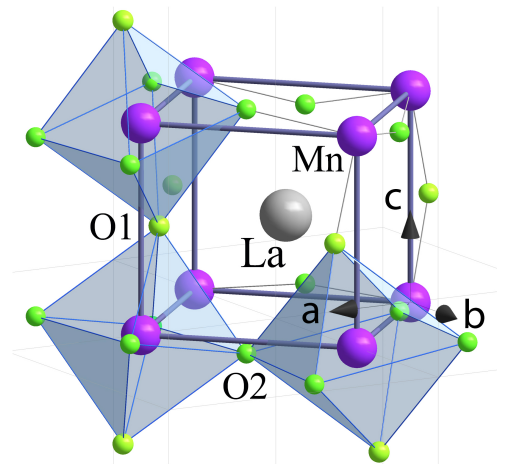


FIG. 1: (Color online) Schematic structure (pseudo-cubic cell) of orthorhombic LaMnO₃ showing O1 and O2 sites.

this static spin order transforms into a time fluctuating short-range spin order of Mn neighbors so that no valuable information on anisotropy of the effective exchange interactions can be obtained above T_N from bulk magnetic and transport measurements of intrinsically-twinned LaMnO_3 crystals [13].

In this paper we resolve issues about the Mn–Mn spin correlations anisotropy and its variation across O' – O transition in LaMnO_3 by means of ^{17}O NMR. In orthorhombic LaMnO_3 there are two structural oxygen sites: O1 and O2 (Fig. 1). The pathway of the SE interaction between two Mn neighbors involves O2 site in the ab -plane and O1 along the c -axis. The nuclear spin, ^{17}I , probes the unpaired electronic spins on the e_g -orbitals through the transferred hyperfine interactions (THI) [14] which scalar part is almost independent of the Mn–Oi–Mn bond bending. The scalar THI traces properties of the SE interaction at each site i.e. in the ab -plane for O2 site and along the c -axis for O1 site. The nuclear spin, ^{139}I , of the La cation probes the electron spin density of the Mn^{3+} ion transferred to the $6s(\text{La})$ orbital through the $\text{Mn}(t_{2g})$ – $\text{O}2(2p_\pi)$ – $\text{La}(6s)$ path [15]. Because of its *eight* Mn^{3+} neighbors the scalar THI traces the SE interaction averaged within the pseudo-cubic cell.

II. EXPERIMENTAL

The preparation and characterization of a stoichiometric LaMnO_3 crystalline sample enriched by ^{17}O NMR isotope up to about 5.5%, was described in [16]. At room temperature, in the $Pbnm$ space group, the lattice parameters are: $a = 5.5379(1)$ Å, $b = 5.7484(1)$ Å, $c = 7.6950(1)$ Å.

The magnetic susceptibility $\chi = M/H$ was measured on a slice of the crystal from $T = 140$ K to 300 K with a SQUID magnetometer (Quantum Design) in a magnetic field $H = 50$ kOe and in the range (295 – 810) K with a Faraday balance technique at $H = 4.5$ kOe.

The ^{17}O and ^{139}La NMR spectra (Fig. 2) were acquired up to 950 K, in a crushed part (~ 200 mesh) of the crystal, with a AVANCE III BRUKER spectrometer operating at $H = 11.7$ T. At this field, the Larmor frequency (ν_L) is 67.800 MHz for ^{17}O (standard H_2O liquid reference) and 70.647 MHz for ^{139}La .

As the quadrupolar interaction is present for ^{17}O ($^{17}\text{I} = 5/2$) and ^{139}La nuclei ($^{139}\text{I} = 7/2$), both spectra are very broad, approximately 2 and 25 MHz, respectively. Although the ^{17}O and ^{139}La spectra overlap, they can be separated and O1, O2 lines can be identified as was described in [16]. As the spectra are broad, a method of frequency sweeping was used. A pulse sequence $\alpha - \tau - 2\alpha - \tau - (\text{echo})$ was used with a delay $\tau = 12$ μs and a pulse duration $\alpha \approx 1$ μs , shorter than the one which optimizes the echo signal amplitude of both nuclei. The total spectrum was obtained by summing the Fourier-transformed half-echo signals acquired at equidistant operating frequencies (step = 0.1 MHz). The sim-

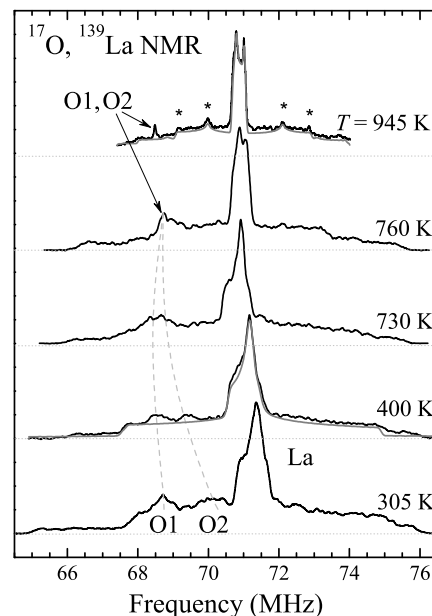


FIG. 2: The ^{17}O and ^{139}La NMR powder spectra of stoichiometric LaMnO_3 ($T_{JT} = 750$ K). The low frequency ^{139}La satellite lines overlap with the O1 and O2 lines. The dotted lines joining O1 peaks and O2 peaks are guide for the eyes. At 945 K, the narrowed satellite peaks of the ^{139}La NMR spectrum are marked by (*). The grey curve beneath the spectrum at $T = 400$ K and 945 K is the corresponding ^{139}La NMR spectrum simulation.

ulation of the ^{139}La quadrupolar split spectra, including both, the central ($m_I = -1/2 \leftrightarrow +1/2$) and the satellite transitions, was performed to determine at each temperature the components of the magnetic shift $\{K_{ii}\}$ as well as the quadrupole frequency $\nu_Q = 3eQV_{zz}/2I(2I - 1)\hbar$ and asymmetry parameter $\eta = |(V_{xx} - V_{yy})/V_{zz}|$ of the electric field gradient (EFG) tensor $\{V_{ii}\}$. The powder pattern simulation program takes into account the quadrupole coupling corrections up to the second order in $\sim \nu_Q/\nu_L$.

The ^{17}O spin echo decay rate, $^{17}T_2^{-1}$, was measured on the peak of each ^{17}O NMR line. The echo-decay data were collected by varying τ . The characteristic time of the echo-decay, $^{17}T_2$, is defined as the time at which the echo-signal $E(2\tau)$ drops to $1/e$ of its starting value.

III. RESULTS AND DISCUSSION

A. Spin and charge environment of La: magnetic susceptibility and ^{139}La NMR

Figure 3a shows the thermal variation of the magnetic susceptibility of a slice of the crystal. The two phase transitions are clearly seen: the onset of the AF ordered phase is displayed as a change of the $\chi(T)$ slope at $T_N \sim 139$ K whereas the upturn at $T_{JT} = 750(2)$ K

indicates the JT transition. In the O' -phase, from 250 K up to 650 K, the magnetic susceptibility follows a Curie-Weiss (C-W) law $\chi(T) = \chi_0 + C/(T - \Theta)$ with a Weiss temperature $\Theta(O'\text{-phase}) = 67(5)$ K and negligible value of $\chi_0 \approx 0.1$ memu/mol. The Curie constant $C = 3.17(10)$ emu · K/mol corresponds to an effective magnetic moment $\mu_{\text{eff}} = 5.04 \mu_B$ which value is only slightly larger than the expected value $\mu_{\text{eff}} = 2\mu_B(S(S+1))^{1/2} = 4.89 \mu_B$ for the $\text{Mn}^{3+}(t_{2g}^3 e_g^1, {}^5E)$ state. Above T_{JT} the C-W law fits well $\chi(T)$ with almost the same C and χ_0 value but with a large positive $\Theta(O\text{-phase}) = 197(5)$ K. The significant increase of Θ on crossing T_{JT} indicates that the Mn-Mn spin correlations are FM-enhanced in the O -phase in agreement with previous χ results [13].

The magnetic shift and EFG parameters of ^{139}La nucleus were deduced from the simulation of the ^{139}La NMR spectra which are represented on Fig. 2 for two selected temperatures, 400 and 945 K. Compared to the O' -phase, the double peaked ^{139}La central line in the O -phase reflects the decrease of η , the asymmetry parameter.

The isotropic magnetic shift, $^{139}K_{\text{iso}} \equiv 1/3Tr\{K_{ii}\}$, scales well the thermal behavior of χ in both phases (Fig. 3b). Indeed, the corresponding local field, $h_{\text{loc}}(\text{La}) = ^{139}K_{\text{iso}}H$, is caused by the Fermi-contact interaction of ^{139}I with the electron spin density $f_{s,\text{La}}\langle s_z(\text{Mn}) \rangle$ transferred at the $6s(\text{La})$ orbital from the eight Mn^{3+} neighbors mainly through the $\text{Mn}(t_{2g})\text{--O}2(2p_\pi)\text{--La}(6s)$ path so that $h_{\text{loc}}(\text{La}) = 8f_{s,\text{La}}H_{FC}(6s)\langle s_z(\text{Mn}) \rangle$. Compared with the bulk susceptibility χ , $^{139}K_{\text{iso}}$ is proportional to the thermal aver-

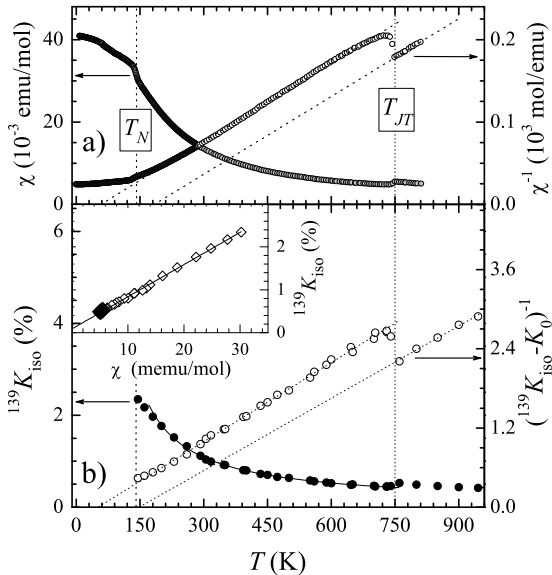


FIG. 3: (a) Magnetic susceptibility $\chi = M/H$ vs T of LaMnO_3 crystal. The dotted lines are the fits to $\chi^{-1}(T)$. (b) ^{139}La isotropic shift, $^{139}K_{\text{iso}}$ vs T (●) and inverse of $(^{139}K_{\text{iso}} - K_0)$ vs T (○). The solid curve is the Curie-Weiss fit for $T < 750$ K, the dotted lines are the fits to $(^{139}K_{\text{iso}} - K_0)^{-1}$. Inset: $^{139}K_{\text{iso}}(\chi)$ plot below 750 K (◇) and above 750 K (◆).

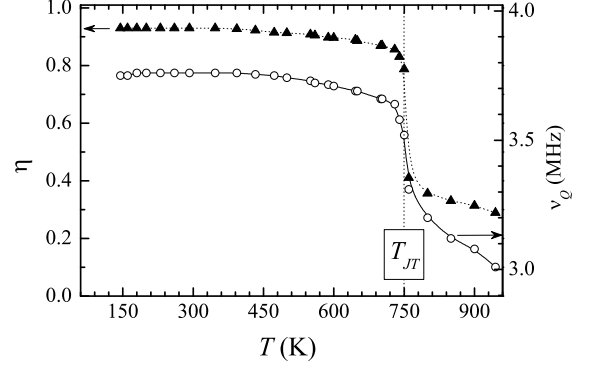


FIG. 4: Thermal behavior of the quadrupolar frequency, $^{139}\nu_Q$ (○), and EFG asymmetry parameter, $^{139}\eta$ (▲), at La site.

aged projection of the Mn spin $\langle s_z(\text{Mn}) \rangle \sim (T - \Theta_{\text{La}})^{-1}$, which reflects the net t_{2g} spin polarization of Mn within each pseudo-cubic unit cell. $^{139}K_{\text{iso}}(T)$ follows also a C-W law: $K_0 + C_{\text{La}}/(T - \Theta_{\text{La}})$ with a T -independent term, $K_0 = 0.07(4)\% \ll ^{139}K_{\text{iso}}(T)$ and $\Theta_{\text{La}}(O') = 55(12)$ K and $\Theta_{\text{La}}(O) = 160(40)$ K. The ^{139}La NMR data confirm that the Mn-Mn exchange coupling becomes more ferromagnetic in the O -phase.

Fig. 4 concerns the charge environment of La cation. In the O' -phase ν_Q and η remain practically unchanged up to about 500 K, smoothly decrease at higher temperature and drop on crossing T_{JT} . The non zero value of the asymmetry parameter, $\eta \approx 0.3$, is in agreement with the symmetry of the O -phase which was found still orthorhombic in the O -phase [4]. The drop of ν_Q and η on crossing T_{JT} , is due to the fact that although there is no change in symmetry, the MnO_6 octahedra become more regular in the O -phase and the observed lattice appears cubic ($a \approx b \approx c/\sqrt{2}$) [4].

It is worth to mention that close to T_{JT} , in the O' and O -phases, all La sites are identical since a single set of the ^{139}La NMR parameters, $\{K_{ii}; V_{ii}\}$, is enough to describe the magnetic and charge environment of La. Therefore, static nanoscale heterogeneities which might appear in LaMnO_3 [17] when approaching T_{JT} from below are not confirmed by ^{139}La NMR.

B. Anisotropy of the Mn-Mn exchange interaction: ^{17}O NMR

^{17}O NMR shed light on the Mn-Mn pair spin correlations which are mainly related to e_g -electron. The covalent electron transfer from its two Mn nearest neighbors creates a fraction of spins, f_s , on the $\text{O}(2s)$ orbital. The hyperfine interaction of ^{17}I with the spin density $f_s\langle s_z(\text{Mn}) \rangle$ results in a local field, $^{17}h_{\text{loc}}$, which is responsible for the large positive shift of the ^{17}O NMR lines. Below 750 K, the NMR powder spectrum consists of two lines, O1, O2 (Fig. 2). The peak posi-

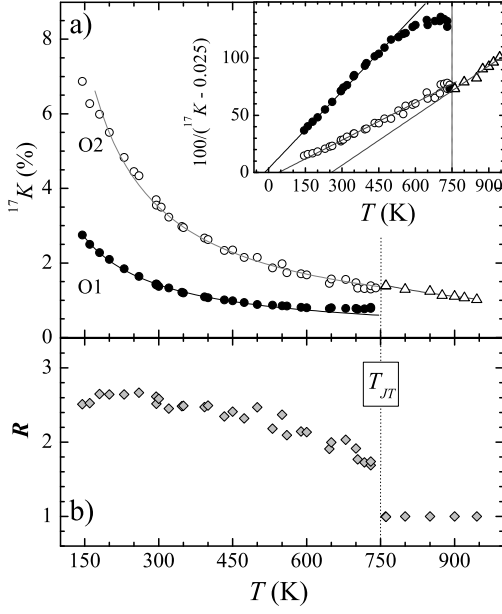


FIG. 5: (a) Oxygen isotropic magnetic shift, ^{17}K vs T for O1 (●) and O2 (○) sites in the O' -phase and for the single magnetic O -site (Δ) in the O -phase. Inset: inverse shift $\{^{17}K - ^{17}K_0\}^{-1}$ vs T . The solid curves are the Curie-Weiss fit to O1 (180 K < T < 550 K), O2 (180 K < T < 750 K) and to the single magnetic O -site above 750 K. (b) Thermal behavior of R , the ratio of the local field created at O2 and at O1 sites by the two Mn nearest neighbors (see text).

tion, ν_p , of the ^{17}O lines defines their isotropic shift $^{17}K = ^{17}h_{\text{loc}}/H = (\nu_p - ^{17}\nu_L)/^{17}\nu_L$, where $^{17}\nu_L$ is the Larmor frequency.

The line displaying the largest ^{17}K was attributed to oxygen atoms in O2 site [16]. From 200 K up to T_{JT} , $^{17}K(T; \text{O2})$ data follow a C-W law: $K_0 + C_{\text{O2}}/(T - \Theta_{\text{O2}})$ with a chemical shift $K_0(\text{O2}) = 0.025(10)\%$ and $\Theta_{\text{O2}} = 35(10)$ K (Fig. 5a). The positive value of Θ_{O2} evidences the FM nature of SE interaction between Mn neighbors in the ab -plane. In contrast to ^{139}La and $^{17}\text{O2}$, the mean field law fits $^{17}K(T; \text{O1})$ data only up to $T^* \sim 550$ K (inset Fig. 5a), with $\Theta_{\text{O1}} = -15(20)$ K and $K_0(\text{O1}) = K_0(\text{O2})$. The slightly negative value of Θ_{O1} demonstrates the AF nature of the interaction between adjacent Mn along c (Mn1 and Mn3 in Fig. 6) resulting from a small imbalance between several SE interaction involving t_{2g} and $e_g(\theta, \varepsilon)$ orbitals [18]. Above T^* , $^{17}K(T; \text{O1})$ deviates from the C-W law and tends towards $^{17}K(T; \text{O2})$. The merging of O1 and O2 NMR lines at the $O'-O$ transition indicates that the two structurally distinct O sites have the same magnetic environment. Above 750 K, the C-W fit of $\{^{17}K(T) - ^{17}K_0\}^{-1}$ yields $K_0 = 0.025(10)\%$ and $\Theta_{\text{O1}, \text{O2}} = 260(50)$ K. Thus ^{17}O NMR demonstrates that the Mn-Mn exchange interaction changes from anisotropic ($\Theta_{\text{O2}} = 35$ K, $\Theta_{\text{O1}} = -15$ K) to isotropic ($\Theta_{\text{O2}} = \Theta_{\text{O1}} = 260$ K) at T_{JT} and that in the O -phase, the isotropic exchange coupling is strongly

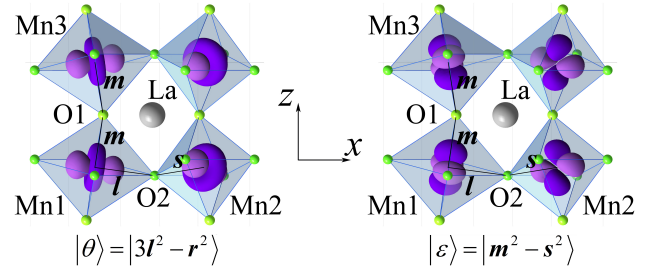


FIG. 6: (Color online) Direction of the e_g -orbitals, $|\theta\rangle$ and $|\varepsilon\rangle$ in the JT distorted MnO_6 octahedra. l , m and s are the long, medium and short Mn-O bond lengths, respectively, x and z are pseudocubic axes.

FM enhanced.

Figure 5b shows the thermal variation of $R = ^{17}h_{\text{loc}}(\text{O2})/^{17}h_{\text{loc}}(\text{O1})$, the ratio of the local field at O2 and O1 sites. R is mainly controlled by the orbital mixing angle φ . In a picture of localized d -electrons, the ground-state wave function of the e_g -electron can be represented as a linear combination of the e_g atomic orbitals: $|\psi_g\rangle = \cos(\varphi/2)|\theta\rangle + \sin(\varphi/2)|\varepsilon\rangle$ for each Mn^{3+} site [2] with φ defined in the pseudocubic axes x , y , z (Fig. 6). We use also the wave function defined in the local coordinates of each Mn site, $|\eta\rangle = c_1|\theta\rangle + c_2|\varepsilon\rangle$, e.g. the $|\theta\rangle$ orbital points in the x direction for Mn1 site. In order to deduce φ , we have calculated $^{17}h_{\text{loc}}(\text{Oi})$ by using an effective Hamiltonian of the super-transferred electron-nuclear interaction:

$$H_{\text{eff}} = \frac{16\pi^{17}\gamma\hbar\mu_B}{3} \sum_{\eta=\theta;\varepsilon} a_{\eta}^{\dagger} a_{\eta} (\langle\eta|2s\rangle + \gamma_{\eta}2s) \times \langle 2s|\mathbf{IS}|2s\rangle (\langle 2s|\eta\rangle + \gamma_{\eta}2s), \quad (1)$$

where the covalent transfer of unpaired electron density is accounted by $\langle 2s|\eta\rangle$, the overlap integrals, and by $\gamma_{\eta}2s$, the covalence parameter. All overlap integrals (Table I) were calculated by using Hartree-Fock's wave functions [19] and atomic positions [4] of the Mn^{3+} and O^{2-} ions. As illustrated in Fig. 6, O1 atom is coupled to Mn1, Mn3 ions via the middle (m) bonds, whereas O2 is connected to Mn1, Mn2 neighbors in ab -plane via the long (l) and short (s) Mn-O bonds. The covalence parameters $\gamma_{\eta}2s$ were assumed to be proportional to the corresponding overlap integrals: $A_{\alpha} \equiv \langle 2s|\theta\rangle_{\alpha}$, $B_{\alpha} \equiv \langle 2s|\varepsilon\rangle_{\alpha}$ ($\alpha = l, m, s$).

Finally, the R -ratio takes the form:

$$R = \frac{c_1^2 A_l^2 + c_1^2 A_s^2 + c_2^2 B_s^2 + 2A_s B_s c_1 c_2}{2[c_1^2 A_m^2 + c_2^2 B_m^2 + 2A_m B_m c_1 c_2]}, \quad (2)$$

where the terms $c_1^2 A_{\alpha}^2$, $c_2^2 B_{\alpha}^2$ are proportional to the conventional spin densities $f_{s,\theta}$, $f_{s,\varepsilon}$ [20] transferred from $|\theta\rangle$ and $|\varepsilon\rangle$ to $\text{O}(2s)$ orbital and the cross term, $\propto c_1 c_2$, describes the quantum interference effect of the interaction (1). The orbital mixing coefficients c_1 , c_2 and φ were estimated with eq. (2) and their value for Mn1

TABLE I: Overlap integrals ($\times 10^{-2}$) between Mn(3d) and O(2s) orbitals calculated for Mn1 site. Indexes $l(x)$, $m(z)$ and $s(y)$ refer to long, middle and short Mn1-O bond, respectively. $\varphi_{\text{nmr}} = 2\pi/3 + 2 \arctan(c_2/c_1)$.

$T(\text{K})$	A_l	A_m	A_s	B_m	B_s	c_1	c_2	φ_{nmr} (degree)
293	3.843	-2.904	-3.263	-5.031	5.651	0.995	-0.10	109(3)
573	3.967	-2.855	-3.208	-4.945	5.557	0.998	-0.06	114(3)
798	5.117	-2.682	-2.795	-4.645	4.840	$c_1 \approx c_2$		~ 90

site are listed at 293 K, 573 K and 798 K in Table I. At 293 K, $R = 2.5 \pm 0.1$ yields $\varphi_{\text{nmr}} = 109 \pm 1.5^\circ$, close to $\varphi_{\text{str}} \sim 108^\circ$ deduced from structural data on Jahn-Teller distorted MnO_6 octahedra in LaMnO_3 [4]. Besides, the cross term $c_1 c_2$ is negative, in agreement with the orthorhombic crystal-field parameters ratio, $E/D = c_1 c_2 / (c_2^2 - c_1^2)$, which was found positive in LaMnO_3 [21] and in an untwined $\text{La}_{0.95}\text{Sr}_{0.05}\text{MnO}_3$ ($T_{JT} \approx 605$ K) single crystal [22]. For $T > T_{JT}$, the fast fluctuations ($t_s \sim 10^{-14}$ sec) of the JT-distorted octahedra [7, 8] are averaged over the time scale of NMR spectra ($t_{\text{nmr}} > 10^{-7}$ sec). Thus, we measure the time-average local magnetic field, $\langle {}^{17}h_{\text{loc}}(\text{Oi}) \rangle_{t_{\text{nmr}}}$. Due to the MnO_6 octahedra fast fluctuations during t_{nmr} , the coherent cross term $\langle c_1 c_2 \rangle_{t_{\text{nmr}}}$ vanishes in eq. (2) yielding $c_1^2 \approx c_2^2 = 0.50(2)$ for $R(798 \text{ K}) = 1.0$. Therefore, for $T > T_{JT}$ and at the time scale t_{nmr} , LaMnO_3 can be described in terms of non-polarized e_g -orbitals, since $|\theta\rangle$ and $|\varepsilon\rangle$ orbitals are equally occupied, in agreement with Ref. [4].

C. Low-frequency dynamics of Mn spin near T_{JT}

The low-frequency dynamics of the Mn spins was studied by measuring the ${}^{17}\text{O}$ spin echo decay rate, T_2^{-1} , on O1 and O2 lines. T_2^{-1} probes the time-dependent fluctuations of the local field ${}^{17}h_{\text{loc}}$ at ${}^{17}\text{O}$ nuclei. The transverse and longitudinal components of ${}^{17}h_{\text{loc}}$, h_\perp and h_\parallel , are defined as a function of the direction of H . In general both h_\perp and h_\parallel contribute to the echo-decay process [23, 24]:

$$T_2^{-1}(T) = {}^{17}\gamma^2 h_\parallel^2 \tau_c + \left({}^{17}I + \frac{1}{2} \right)^2 T_1^{-1}(T), \quad (3)$$

where the nuclear spin-lattice relaxation rate, T_1^{-1} , involves only the transverse components, probing $\langle h_\perp(0)h_\perp(t) \rangle$. Usually at elevated temperature far above the magnetic transition, the second term in (3) dominates and the contribution to the ${}^{17}\text{O}$ echo decay rate [25] at Oi site is:

$$T_{2,i}^{-1}(T) \propto \left({}^{17}I + \frac{1}{2} \right)^2 [f_s H_{FC}(2s) A_q(\text{Oi})]^2 T \chi_i(T), \quad (4)$$

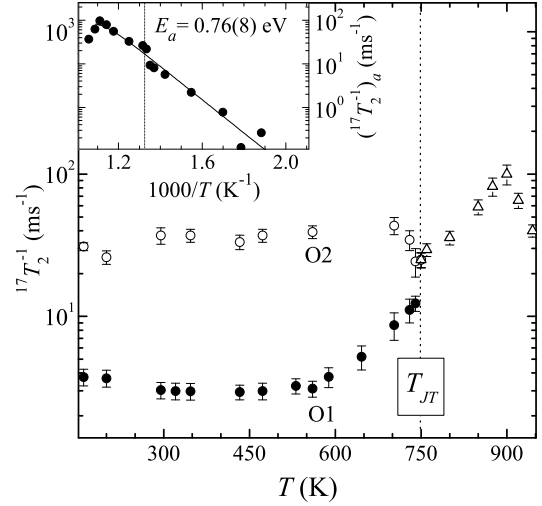


FIG. 7: Thermal behavior of ${}^{17}\text{O}$ echo decay rate, ${}^{17}T_2^{-1}$ for O1 (\bullet) and O2 (\circ) sites in the O' -phase and for the single magnetic O -site (\triangle) in the O -phase. Inset: thermally activated component $({}^{17}T_2^{-1})_a = \{ {}^{17}T_2^{-1}(T) - {}^{17}T_2^{-1}(293 \text{ K}) \}$ versus $1000/T$.

where χ_i is the local spin susceptibility of Mn ions in the ab -plane ($i = 2$) and along c -axis ($i = 1$), it is proportional to ${}^{17}K(T; \text{Oi})$. The factor $f_s H_{FC}(2s)$ is the local field created at the ${}^{17}\text{O}$ nucleus by the unpaired spin of one Mn neighbor, f_s is the spin density transferred from e_g to O(2s) orbital and $H_{FC}(2s)$ is the Fermi contact field of the O(2s) orbital. The form-factors $A_q(\text{Oi})$ takes into account the FM correlations of the Mn neighbours in the ab -plane ($A_q^2(\text{O2}) = 1$) and the AF correlations along the c -axis ($A_q^2(\text{O1}) < 1$).

The data on Figure 7 show that as long as the mean field behavior holds for ${}^{17}K(T; \text{Oi})$ i.e. as long as $\chi_i(T)$ is proportional to $(T - \Theta_i)^{-1}$, $T_2^{-1}(\text{Oi})$ is almost T -independent above room temperature in agreement with expression (4). Indeed, $T_2^{-1}(\text{O2})$ is constant up to $T \approx T_{JT}$ whereas $T_2^{-1}(\text{O1})$ is constant only up to 560 K that is, up to $\sim T^*$. Above T^* , $T_2^{-1}(\text{O1})$ starts to increase and approaches $T_2^{-1}(\text{O2})$ values close to T_{JT} . In the O -phase, T_2^{-1} displays a maximum near 900 K. This behaviour reflects the thermal activation of an additional fluctuating mechanism which becomes visible for O1 site, above T^* . Its prominent contribution, $(T_2^{-1})_a$, to $T_2^{-1}(T)$ is defined as the difference $(T_2^{-1})_a = T_2^{-1}(T) - T_2^{-1}(293 \text{ K})$. As seen in the inset of Fig. 7, $(T_2^{-1})_a$ has an exponential behavior versus $1/T$ below 900 K. We model this mechanism with the correlation function $\langle h_\perp(0)h_\perp(t) \rangle = h_\perp(0)^2 \exp(-t/\tau_c)$ which yields $(T_2^{-1})_a \propto h_\perp(0)^2 \tau_c / [1 + (\omega_L \tau_c)^2]$, where τ_c is the correlation time characterizing fluctuations of $h_\perp(t)$ and ${}^{17}\omega_L = 2\pi\nu_L$. Assuming that $\tau_c = \tau_{c0} \exp(E_a/T)$, the model reproduces the main experimental features i.e. for $\omega_L \tau_c \gg 1$, $(T_2^{-1})_a$ scales τ_c^{-1} and $(T_2^{-1})_a$ reaches a maximum at $\omega_L \tau_c \sim 1$. The deduced energy barrier, $E_a = 0.76(8) \text{ eV}$, is consistent with estimates of Δ_{JT} ,

the JT splitting of the e_g state, $0.7 < \Delta_{JT} < 0.9$ eV [6, 26, 27].

As the deduced value, $\tau_{c0} = 1.2(2) \cdot 10^{-12}$ sec, is too large to describe a vibrating MnO_6 octahedron [7, 8], we speculate that some collective modes of adjacent octahedra [9, 10] are responsible for the Mn spin slow fluctuations below and above T_{JT} . To date we are not able to specify all the parameters of these modes. Nevertheless, the propagation vector should be directed along the c -axis, providing above T^* a melting mechanism of the AF spin correlations between adjacent Mn in this direction. Moreover, according to the ^{139}La NMR results, the MnO_6 octahedra should fluctuate in such a correlated manner that their averaged effect results in an asymmetric charge environment of La atoms (Fig. 4). Even in the O -phase with a metrically cubic ($a \approx b \approx c/\sqrt{2}$) lattice [4] the structural position of La remains aside the inversion symmetry point $\{0;0;0\}$ of the pseudo-cubic unit cell shown in Fig. 1.

IV. CONCLUSION

We have studied the long-range orbital order and its melting as well as the $\text{Mn}^{3+}\text{-O-Mn}^{3+}$ exchange interaction in the paramagnetic O' -phase and above $T_{JT} = 750$ K, in the O -phase of a stoichiometric LaMnO_3 crystalline sample.

At 293 K, the orbital mixing angle of the ground state wave function of the e_g -electron, $\varphi_{\text{nrmr}} = 109 \pm 1.5^\circ$, was obtained from ^{17}O NMR. This value is close to $\varphi_{\text{str}} = 108^\circ$, deduced from structural data based on the Jahn-Teller distortions of the MnO_6 octahedra [4]. The fact that φ_{nrmr} is close to φ_{str} supports the theoretical works [5, 6, 27] which conclude that both, the SE interactions $e\text{-}e$ and the JT distortions $e\text{-}l$ are needed to explain the orbital ordering. In the orbital fluctuating O -phase the NMR data which correspond to a time averaged orbital configurations yield equally weighted orbitals for the e_g -doublet. Not so many experimental methods are able to yield the orbital mixing angle and this ^{17}O NMR approach could be extended to other strongly correlated oxide materials with an active orbital degree of freedom.

The two distinct oxygen sites of the structure enable to

probe different Mn-Mn spin correlations; O2 sites probe the Mn-Mn spin correlations in the ab -plane whereas O1 sites probe the Mn-Mn spin correlations along the c -axis. In the O' -phase, the NMR properties measured at O2 site are robust up to the transition temperature, T_{JT} , while at O1 site they show a marked change below T_{JT} , at about $T^* = 550$ K. Indeed, the ferromagnetic nature of the superexchange coupling, SE, between Mn spins in the ab -plane is confirmed up to T_{JT} whereas along the c -axis, SE is antiferromagnetic up to T^* and alters gradually toward FM-type with further heating, resulting in an anisotropic-to-isotropic change of the exchange coupling with reinforced ferromagnetic correlations above T_{JT} . Furthermore, the ^{17}O spin-spin relaxation time, $^{17}T_2$, which shed light on the low frequency dynamics of the Mn spins, shows also different behavior at O2 and O1 sites. Indeed at O2 site, $^{17}T_2(\text{O2})$ is constant up to T_{JT} while at O1 sites $^{17}T_2(\text{O1})$ data evidence that above T^* , slow fluctuations of the Mn spins along c are thermally activated. Collective modes of adjacent octahedra along the c -axis should be considered for this slow mechanism which yields changes of the spin correlations between adjacent Mn along c , a spin marker of the orbital ordering.

It is worth to note that at about 600 K, close to T^* , a change in slope of the thermal behavior of the resistivity of LaMnO_3 was interpreted as the onset of orbital-disorder fluctuations [17]. Nevertheless, static nanoscale charge and spin heterogeneities which might appear in such a scenario of the 3D-melting of the orbital order in LaMnO_3 when approaching T_{JT} from below are not confirmed by ^{139}La NMR. Our ^{17}O NMR results show that T^* marks rather a 3D to 2D crossover since only the magnetic coupling between Mn neighbors in adjacent ab -layers alters and thus T^* marks the onset of a melting of the long-range orbital order along the c -axis.

ACKNOWLEDGEMENTS

We acknowledge Dm. Korotin for fruitful discussion of the DMFT results in LaMnO_3 . This work is supported in part by the RFBR Grant No 12-02-00358 and the UB RAS Research Projects Ns 12-M-23-2061; 12-Y-2-1025. S.V. and A.G. thank ESPCI for hospitality and support.

-
- [1] M. B. Salamon and M. Jaime, Rev. Mod. Phys. **73**, 583 (2001).
 - [2] K. I. Kugel and D. I. Khomskii, Sov. Phys. JETP **37**, 725 (1973).
 - [3] J. Kanamori, J. Appl. Phys. **31**, S14 (1960).
 - [4] J. Rodriguez-Carvajal, M. Hennion, F. Moussa, A. H. Moudden, L. Pinsard, and A. Revcolevschi, Phys. Rev. B **57**, R3189 (1998).
 - [5] I. Leonov, D. Korotin, N. Binggeli, V. I. Anisimov, and D. Vollhardt, Phys. Rev. B **81**, 075109 (2010).
 - [6] E. Pavarini and E. Koch, Phys. Rev. Lett. **104**, 086402 (2010).
 - [7] E. Granado, J. A. Sanjurjo, C. Rettori, J. J. Neumeier, and S. B. Oseroff, Phys. Rev. B **62**, 11304 (2000).
 - [8] L. Martin-Carron and A. de Andres, Eur. Phys. J. B **22**, 11 (2001).
 - [9] M. C. Sanchez, G. Subias, J. Garcia, and J. Blasco, Phys. Rev. Lett. **90**, 045503 (2003).
 - [10] X. Qiu, T. Proffen, J. F. Mitchell, and S. J. L. Billinge, Phys. Rev. Lett. **94**, 177203 (2005).
 - [11] J. B. Goodenough, Phys. Rev. **100**, 564 (1955).
 - [12] F. Moussa, M. Hennion, J. Rodriguez-Carvajal,

- H. Moudden, L. Pinsard, and A. Revcolevschi, Phys. Rev. B **54**, 15149 (1996).
- [13] J. S. Zhou and J. B. Goodenough, Phys. Rev. B **60**, R15002 (1999).
- [14] A. Trokiner, A. Yakubovskii, S. Verkhovskii, A. Gerashenko, and D. Khomskii, Phys. Rev. B **74**, 092403 (2006).
- [15] Y. Yoshinari, P. C. Hammel, J. D. Thompson, and S.-W. Cheong, Phys. Rev. B **60**, 9275 (1999).
- [16] L. Pinsard-Gaudart, A. Trokiner, S. Verkhovskii, A. Gerashenko, and N. Dragoe, Solid State Communications **151**, 1968 (2011).
- [17] J. S. Zhou and J. B. Goodenough, Phys. Rev. B **68**, 144406 (2003).
- [18] J. S. Zhou and J. B. Goodenough, Phys. Rev. Lett. **96**, 247202 (2006).
- [19] E. Clementi and L. Roetti, At. Data Nucl. Data tables **14**, 177 (1974).
- [20] J. Owen and J. H. M. Thornley, Rep. Prog. Phys. **29**, 675 (1966).
- [21] G. Matsumoto, J. Phys. Soc. Jpn **29**, 606 (1970).
- [22] J. Deisenhofer, M. V. Eremin, D. V. Zakharov, V. A. Ivanshin, R. M. Eremina, H.-A. Krug von Nidda, A. A. Mukhin, A. M. Balbashov, and A. Loidl, Phys. Rev. B **65**, 104440 (2002).
- [23] C. Slichter, *Principles of Magnetic Resonance* (Springer-Verlag, Berlin, 1990), p. 640.
- [24] R. E. Walstedt, Phys. Rev. Lett. **19**, 146 (1967).
- [25] T. Moriya, Prog. Theor. Phys. **16**, 641 (1956).
- [26] N. N. Kovaleva, A. V. Boris, C. Bernhard, A. Kulakov, A. Pimenov, A. M. Balbashov, G. Khaliullin, and B. Keimer, Phys. Rev. Lett. **93**, 147204 (2004).
- [27] W. G. Yin, D. Volja, and W. Ku, Phys. Rev. Lett. **96**, 116405 (2006).